Geophys. J. Int. (2006) **165,** 596–606 doi: 10.1111/j.1365-246X.2006.02937.x

Polarization analysis and polarization filtering of three-component signals with the time–frequency *S* transform

C. R. Pinnegar

Calgary Scientific, Inc., Unit 208, 1210-20 *Ave. SE, Calgary, Alberta, Canada. E-mail: pinnegar@ucalgary.ca*

Accepted 2006 January 19. Received 2005 September 6; in original form 2003 September 29

SUMMARY

From basic Fourier theory, a one-component signal can be expressed as a superposition of sinusoidal oscillations in time, with the Fourier amplitude and phase spectra describing the contribution of each sinusoid to the total signal. By extension, three-component signals can be thought of as superpositions of sinusoids oscillating in the **x**-, **y**-, and **z**-directions, which, when considered one frequency at a time, trace out elliptical motion in three-space. Thus the total three-component signal can be thought of as a superposition of ellipses. The information contained in the Fourier spectra of the **x**-, **y**-, and **z**-components of the signal can then be re-expressed as Fourier spectra of the elements of these ellipses, namely: the lengths of their semi-major and semi-minor axes, the strike and dip of each ellipse plane, the pitch of the major axis, and the phase of the particle motion at each frequency. The same type of reasoning can be used with windowed Fourier transforms (such as the *S* transform), to give time-varying spectra of the elliptical elements. These can be used to design signal-adaptive polarization filters that reject signal components with specific polarization properties. Filters of this type are not restricted to reducing the whole amplitude of any particular ellipse; for example, the 'linear' part of the ellipse can be retained while the 'circular' part is rejected. This paper describes the mathematics behind this technique, and presents three examples: an earthquake seismogram that is first separated into linear and circular parts, and is later filtered specifically to remove the Rayleigh wave; and two shot gathers, to which similar Rayleigh-wave filters have been applied on a trace-by-trace basis.

Key words: particle motion, polarization analysis, polarization filtering, spectral analysis, time–frequency analysis, wavelets.

1 INTRODUCTION

In geophysical time series analysis one must often deal with three-component signals. Some examples are measurements of time-varying electric and magnetic fields, and three-component seismograms. Since the 1960s, several methods have been advanced to describe the content of time series of this type, usually with a view to seismic interpretation and filtering of seismograms based on the polarization properties of different types of waves (for discussions of these properties see Aki & Richards 1980; Kanasewich 1981; Lay & Wallace 1995). Most of these techniques operate entirely in the time domain (Flinn 1965; Montalbetti & Kanasewich 1970; Vidale 1986; Morozov & Smithson 1996), or entirely in the frequency domain (Simons 1968; Samson & Olson 1980). In real seismograms, though, events that have different frequencies and different polarization characteristics can occur at the same time; also, any particular frequency band may at two different times be dominated by events that do not have the same polarization properties.

This paper presents a method of describing time and frequency variations in the polarization properties of non-stationary three-component signals. The method makes use of the *S* transform (Stockwell *et al.* 1996), a time–frequency spectral localization method that is similar to the short-time Fourier transform (STFT) (Gabor 1946; Cohen 1995) except that its window scales with frequency, as wavelets do (Grossmann & Morlet 1984; Mallat 1998). The use of a translatable window gives some similarities with the 'moving window' techniques used to analyse surface waves in the 1970s (Flinn 1965; Montalbetti & Kanasewich 1970); the scalability of the window, and the provision for both time and frequency dependence of polarization, are reminiscent of the methods outlined by Jurkevics (1988), Lilly & Park (1995), Anant & Dowla (1997), Zanandrea *et al.* (2000), and Claassen (2001). Unlike these techniques, though, the *S*-transform method does not involve covariance matrices or singular-value decomposition. Instead, the polarization characteristics of the data are calculated directly from the complex *S* transforms of the separate **x**, **y**, and **z** data components. In this regard there is some conceptual similarity with the Hilbert transform approach used by Morozov & Smithson (1996), but with explicit frequency dependence of polarization.

The method is easiest to understand if one first considers the discrete Fourier transforms (DFTs) of the different components of the time series. The fth complex coefficient of the DFT of each individual component can be thought of as giving the amplitude and phase of a 1-D sinusoidal oscillation, whose frequency is determined by f. When the DFTs of all three components are considered together, their fth complex coefficients give the amplitudes and phases of three sinusoidal oscillations in the **x**, **y**, and **z** directions, all of which have the same frequency. This gives elliptically polarized motion in 3-space. The elements of this ellipse, and of the similar ellipses constructed at other values of f, can be plotted as functions of frequency to provide a different set of Fourier spectra. The phase spectrum is retained, but the traditional amplitude spectrum is replaced with spectra of the semi-major and semi-minor axes of the ellipse. Also, three new spectra describe the orientation of the ellipse at each frequency.

The same methodology can be used to give polarization ellipses that depend on both time and frequency by substituting a time–frequency distribution, such as the STFT or the S transform, in place of the DFT. (Here the S transform is preferable to the STFT because the scalable S-transform window ensures that the same number of cycles of Fourier sinusoid are used to obtain local polarization properties at each time and each frequency. This avoids some resolution problems of the STFT that are due to the fixed width of its window.) The resulting time–frequency spectra of the elliptical elements can then be used to design signal-adaptive time–frequency filters which target parts of the signal that have specific polarization properties. The filtering operation does not necessarily have to involve reducing the amplitude of the entire ellipse; for example, the 'circular' part of the ellipse can be removed while its 'linear' part is retained. This type of approach to polarization analysis and filtering of seismic waves has not been used before.

Readers who are already familiar with time–frequency analysis and who wish to proceed directly to an example without going through the mathematical details can skip most of Section 2. It is only necessary to read the definitions of the Fourier-domain forms of the spectra of the elliptical elements $a(f), \ldots, \varphi(f)$ at the start of Section 2.4, and to understand that (as described in the preceding paragraph) in the actual technique these are replaced with $a[\hat{\tau}, \hat{f}], \ldots, \varphi[\hat{\tau}, \hat{f}]$, analogous functions of discrete time and frequency that describe the time evolution of the size, shape, orientation, and phase of the polarization ellipse at each discrete frequency.

2 THEORY

For purposes of clarity, and to define a number of quantities that are used later on, we begin by summarizing the basic properties of the Fourier transform and the S transform.

2.1 Summary of the Fourier transform

If x, a function of a continuous time variable t, and X, a function of a continuous frequency variable f, constitute a Fourier transform pair, then the mathematical relationship between x and X is described by the well known equations

$$X(f) = \int_{-\infty}^{\infty} x(t)\ \exp(-2\pi i f t)\, dt, \tag{1}$$

$$x(t) = \int_{-\infty}^{\infty} X(f)\ \exp(+2\pi i f t)\, df. \tag{2}$$

In general, $X(f)$ is complex-valued. Its content can be expressed in terms of two real-valued functions, $X_R(f)$ and $X_I(f)$, the real and imaginary parts of $X(f)$,

$$X(f) = X_R(f) + i X_I(f). \tag{3}$$

For our purposes it can safely be assumed that $x(t)$ is real since $x(t)$ denotes a measurable physical quantity. Given this assumption, it is not difficult to show that $X(f) = X^*(-f)$ (the asterisk denotes complex conjugation), which allows us to rearrange eq. (2) to

$$x(t) = 2\int_0^{\infty} X_R(f)\ \cos(2\pi f t) - X_I(f)\ \sin(2\pi f t)\, df. \tag{4}$$

Combining the cosine and sine terms from the integrand of eq. (4) into a single, phase-shifted cosine term gives an alternative representation of $x(t)$,

$$x(t) = 2\int_0^{\infty} X_A(f)\ \cos[2\pi f t - X_\Phi(f)], \tag{5}$$

where

$$\begin{aligned} X_A(f) &= \sqrt{[X_R(f)]^2 + [X_I(f)]^2}, \\ X_\Phi(f) &= \arctan\left(\frac{-X_I(f)}{X_R(f)}\right). \end{aligned} \tag{6}$$

The quantities $X_A(f)$ and $X_\Phi(f)$ are referred to as the amplitude and phase spectra of $X(f)$. [In eq. (6) and subsequent equations, 'arctan' denotes the four-quadrant inverse tangent function when the argument is a fraction.] The advantage of eq. (5) over eq. (4) is that the contribution any particular frequency makes to $x(t)$ is expressed in terms of the properties of a single function of time [the phase-shifted cosine in the integrand of eq. (5)] instead of the properties of two different functions [the cosine and sine terms in the integrand of eq. (4)], which makes eq. (5) preferable for intuitive interpretation.

2.2 The continuous-time *S* transform

A disadvantage of the Fourier transform is that $x(t)$ is represented in terms of infinite sinusoids that have no time localization. Thus the Fourier transform is poorly suited to describing local spectral content. To this end, several methods of localizing $X(f)$ in time to produce a time–frequency spectrum $X(\tau, f)$ (here τ denotes the time of localization) have been published over the last few decades. These include the STFT and the continuous wavelet transforms (CWTs). A time–frequency distribution that combines the advantages of the STFT and CWTs is the S transform (Stockwell *et al.* 1996), defined by

$$\begin{aligned} X(\tau, f) = \int_{-\infty}^{\infty} x(t) &\left\{\frac{|f|}{\sqrt{2\pi}} \exp\left[\frac{-f^2(\tau - t)^2}{2}\right]\right\} \\ &\times \exp(-2\pi i f t)\, dt. \end{aligned} \tag{7}$$

The analysing window of the S transform is a Gaussian whose standard deviation is always equal to one wavelength of the Fourier sinusoid. The scaled, wavelet-like S-transform window gives a multiresolution analysis that retains the absolute phase reference of the STFT. Like the Fourier transform, $X(\tau, f)$ has real and imaginary parts $X_R(\tau, f)$ and $X_I(\tau, f)$, and amplitude and phase S spectra $X_A(\tau, f)$ and $X_\Phi(\tau, f)$, whose definitions are analogous with eqs (3) and (6). Effectively, $X_A(\tau, f)$ and $X_\Phi(\tau, f)$ can be thought of as the local amplitude and phase of the contribution that the frequency f makes to $x(t)$, as measured within a few Fourier wavelengths of $t = \tau$.

An alternative expression of $X(\tau, f)$, obtained from eq. (7) using the convolution theorem, is (Stockwell *et al.* 1996):

$$X(\tau, f) = \int_{-\infty}^{\infty} X(\alpha + f) \exp\left(\frac{-2\pi^2\alpha^2}{f^2}\right) \exp(2\pi i \alpha \tau)\, d\alpha. \quad (8)$$

Here α has the same units as f.

One important property of the S transform is invertibility; it converges to $X(f)$ when integrated over all values of τ,

$$\int_{-\infty}^{\infty} X(\tau, f)\, d\tau = X(f). \quad (9)$$

2.3 Three-component functions

Suppose now that $x(t)$ is the **x**-component of a three-component vector-valued function of time, $\mathbf{r}(t)$, whose **y**- and **z**-components are denoted $y(t)$ and $z(t)$, so that

$$\mathbf{r}(t) = \{x(t), y(t), z(t)\}. \quad (10)$$

By analogy with eqs (1)–(4), $y(t)$ and $z(t)$ have Fourier transforms $Y(f)$ and $Z(f)$, whose real and imaginary parts are $Y_R(f)$, $Y_I(f)$, $Z_R(f)$, and $Z_I(f)$. From eqs (4) and (10),

$$\begin{aligned}\mathbf{r}(t) &= 2\int_0^{\infty} \mathbf{r}_f(t)\, df,\\ \mathbf{r}_f(t) &= \{X_R(f)\, \cos(2\pi ft) - X_I(f)\, \sin(2\pi ft),\\ &\quad Y_R(f)\, \cos(2\pi ft) - Y_I(f)\, \sin(2\pi ft),\\ &\quad Z_R(f)\, \cos(2\pi ft) - Z_I(f)\, \sin(2\pi ft)\}. \end{aligned} \quad (11)$$

Here $\mathbf{r}_f(t)$ denotes the contribution that the frequency f makes to $\mathbf{r}(t)$. It is also possible to express eq. (10) in terms of $X_A(f)$ and $X_\Phi(f)$, and the amplitude and phase spectra of $Y(f)$ and $Z(f)$ [defined by analogy with eqs (5) and (6)] through

$$\begin{aligned}\mathbf{r}(t) &= 2\int_0^{\infty} \mathbf{r}_f(t)\, df,\\ \mathbf{r}_f(t) &= \{X_A(f)\, \cos[2\pi ft - X_\Phi(f)],\\ &\quad Y_A(f)\, \cos[2\pi ft - Y_\Phi(f)],\\ &\quad Z_A(f)\, \cos[2\pi ft - Z_\Phi(f)]\}\, df. \end{aligned} \quad (12)$$

However, eq. (12) does not provide much advantage for interpretation as compared with eq. (11) because, in eq. (12), the content of $\mathbf{r}_f(t)$ is expressed in terms of the properties of three different functions (the phase-shifted cosines oscillating in the **x**, **y** and **z** directions). For intuitive purposes, it is desirable to find a way of expressing $\mathbf{r}_f(t)$ in terms of the properties of a single function of time; this objective is very similar to that which led us to rewrite eq. (4) as eq. (5).

2.4 Spectra of the elliptical elements

One solution to the problem described in Section 2.3 is to treat the oscillating amplitudes of the **x**, **y** and **z** Fourier sinusoids of any particular frequency f as time-dependent vector coordinates of an ellipse being traced out in 3-space. The elements of this ellipse uniquely describe the contribution of the fth frequency to the total signal. These are:

(1) $a(f)$, the semi-major axis of the ellipse ($a(f) \geq 0$).

(2) $b(f)$, the semi-minor axis of the ellipse ($a(f) \geq b(f) \geq 0$).

(3) $I(f)$, the inclination of the ellipse to the horizontal (**x**, **y**) plane ($0 < I(f) < \pi$). If $I(f) < \pi/2$, the particle motion is counter-clockwise as viewed from a position having large displacement in the positive **z**-direction; if $I(f) > \pi/2$, the particle motion is clockwise. $I(f)$ can be thought of as the 'dip' of the ellipse plane.

(4) $\Omega(f)$, the azimuth of the ascending node (the point at which the function crosses the (**x**, **y**) plane in the positive **z**-direction), measured counter-clockwise from {1, 0, 0} ($-\pi < \Omega(f) < \pi$). $\Omega(f)$ can be thought of as the 'strike' of the ellipse plane.

(5) $\omega(f)$, the angle between the ascending node and the position of maximum displacement ($0 < \omega(f) < \pi$). $\omega(f)$ can be thought of as the 'pitch' of the major axis of the ellipse.

(6) $\varphi(f)$, the phase, measured with respect to the time of maximum displacement ($-\pi < \varphi(f) < \pi$).

There are of course two positions of maximum displacement; the definitions of $\omega(f)$ and $\varphi(f)$ refer to the position of maximum displacement that has a positive **z** coordinate. It should be kept in mind that, although $I(f)$, $\Omega(f)$ and $\omega(f)$ do essentially represent dip, strike and pitch, their definitions also have to account for clockwise versus counter-clockwise motion which leads to some differences from the normal definitions of these quantities.

To obtain the expressions of $a(f), \ldots, \varphi(f)$ in terms of $X_R(f), \ldots, Z_I(f)$, it is necessary to derive $X_R(f), \ldots, Z_I(f)$ in terms of $a(f), \ldots, \varphi(f)$ and invert the result. This is done by defining a parametric path, denoted $\mathbf{r}'(t)$, that traces out an ellipse in 3-space,

$$\mathbf{r}'(t) = \{a(f)\, \cos[2\pi ft - \varphi(f)], b(f)\, \sin[2\pi ft - \varphi(f)], 0\}. \quad (13)$$

Here f is any frequency, and $a(f)$, $b(f)$, $\varphi(f)$ satisfy the above-listed constraints. Then an arbitrarily oriented elliptical path $\mathbf{r}_f(t)$ can be derived by subjecting $\mathbf{r}'(t)$ to three rotations:

(1) a counter-clockwise rotation through $\omega(f)$ about the z-axis, described by the matrix

$$P_1 = \begin{pmatrix} \cos\omega(f) & -\sin\omega(f) & 0 \\ \sin\omega(f) & \cos\omega(f) & 0 \\ 0 & 0 & 1 \end{pmatrix}; \quad (14)$$

(2) a counter-clockwise rotation through $I(f)$ about the x-axis, described by the matrix

$$P_2 = \begin{pmatrix} 1 & 0 & 0 \\ 0 & \cos I(f) & -\sin I(f) \\ 0 & \sin I(f) & \cos I(f) \end{pmatrix}; \quad (15)$$

and

(3) a counter-clockwise rotation through $\Omega(f)$ about the z-axis, described by the matrix

$$P_3 = \begin{pmatrix} \cos\Omega(f) & -\sin\Omega(f) & 0 \\ \sin\Omega(f) & \cos\Omega(f) & 0 \\ 0 & 0 & 1 \end{pmatrix}. \quad (16)$$

Then

$$\mathbf{r}_f(t) = P_3 P_2 P_1 \mathbf{r}'(t). \quad (17)$$

When the resulting $\mathbf{r}_f(t)$ is compared with eq. (11), the following expressions for $X_R(f), \ldots, Z_I(f)$ are obtained:

$$\begin{aligned}
X_R(f) &= a(f)\ \cos\varphi(f)\{\ \cos\omega(f)\cos\Omega(f)\\
&\qquad - \sin\omega(f)\sin\Omega(f)\cos I(f)\}\\
&\quad +b(f)\ \sin\varphi(f)\{\ \sin\omega(f)\cos\Omega(f)\\
&\qquad + \cos\omega(f)\sin\Omega(f)\cos I(f)\}\\
X_I(f) &= b(f)\ \cos\varphi(f)\{\ \sin\omega(f)\cos\Omega(f)\\
&\qquad + \cos\omega(f)\sin\Omega(f)\cos I(f)\}\\
&\quad -a(f)\ \sin\varphi(f)\{\ \cos\omega(f)\cos\Omega(f)\\
&\qquad - \sin\omega(f)\sin\Omega(f)\cos I(f)\}\\
Y_R(f) &= a(f)\ \cos\varphi(f)\{\ \cos\omega(f)\sin\Omega(f)\\
&\qquad + \sin\omega(f)\cos\Omega(f)\cos I(f)\}\\
&\quad +b(f)\ \sin\varphi(f)\{\ \sin\omega(f)\sin\Omega(f)\\
&\qquad - \cos\omega(f)\cos\Omega(f)\cos I(f)\}\\
Y_I(f) &= b(f)\ \cos\varphi(f)\{\ \sin\omega(f)\sin\Omega(f)\\
&\qquad - \cos\omega(f)\cos\Omega(f)\cos I(f)\}\\
&\quad -a(f)\ \sin\varphi(f)\{\ \cos\omega(f)\sin\Omega(f)\\
&\qquad + \sin\omega(f)\cos\Omega(f)\cos I(f)\}\\
Z_R(f) &= a(f)\ \cos\varphi(f)\quad \sin\omega(f)\sin I(f)\\
&\quad -b(f)\ \sin\varphi(f)\quad \cos\omega(f)\sin I(f)\\
Z_I(f) &= -a(f)\ \sin\varphi(f)\ \sin\omega(f)\sin I(f)\\
&\quad -b(f)\ \cos\varphi(f)\quad \cos\omega(f)\sin I(f)
\end{aligned} \tag{18}$$

Substitution of eq. (18) into eq. (11) gives the contribution of frequency f to $\mathbf{r}(t)$ in terms of $a(f), \ldots, \varphi(f)$. The quantities $a(f), \ldots, \varphi(f)$ are similar to the osculating elements of planetary orbits (Murray & Dermott 1999), but the properties of the ellipse are different from a planetary orbit because $\{0, 0, 0\}$ occurs at the centre of the ellipse instead of at a focus of the ellipse (also, the particle motion is harmonic which differs from planetary motion).

The inversion of expression (18) to give $a(f), \ldots, \varphi(f)$ in terms of $X_R(f), \ldots, Z_I(f)$ requires very long derivations, so only the results are presented here. For brevity,

$$\begin{aligned}
A &= X_R^2 + X_I^2 + Y_R^2 + Y_I^2 + Z_R^2 + Z_I^2,\\
B &= X_R^2 - X_I^2 + Y_R^2 - Y_I^2 + Z_R^2 - Z_I^2,\\
C &= -2(X_R X_I + Y_R Y_I + Z_R Z_I).
\end{aligned} \tag{19}$$

Then

$$\begin{aligned}
a &= \frac{1}{\sqrt{2}}\sqrt{A + \sqrt{B^2 + C^2}},\\
b &= \frac{1}{\sqrt{2}}\sqrt{A - \sqrt{B^2 + C^2}},\\
I &= \arctan\left\{\frac{\left[(Z_R Y_I - Z_I Y_R)^2 + (Z_R X_I - Z_I X_R)^2\right]^{1/2}}{(Y_R X_I - Y_I X_R)}\right\},\\
\Omega &= \arctan\left\{\frac{(Z_R Y_I - Z_I Y_R)}{(Z_R X_I - Z_I X_R)}\right\},\\
\omega &= \omega_0 - \pi\left(\frac{\mathrm{sign}(\omega_0) - 1}{2}\right),
\end{aligned}$$

where

$$\begin{aligned}
\omega_0 &= \arctan\left\{\frac{b[Z_R\cos(\varphi_0) - Z_I\sin(\varphi_0)]}{-a[Z_R\sin(\varphi_0) + Z_I\cos(\varphi_0)]}\right\},\\
\varphi &= \varphi_0 + \pi\left(\frac{\mathrm{sign}(\omega_0) - 1}{2}\right)\mathrm{sign}(\varphi_0),
\end{aligned}$$

where

$$\varphi_0 = \frac{1}{2}\arctan\left(\frac{C}{B}\right). \tag{20}$$

The (f) arguments have been deliberately omitted from eqs (19) and (20) to generalize these expressions; this will be discussed in the next section.

2.5 Discrete time

In most practical applications $\mathbf{r}(t)$ is known only through a sampled time series $\mathbf{r}[\hat{t}]$, defined by

$$\mathbf{r}[\hat{t}] = \{x[\hat{t}], y[\hat{t}], z[\hat{t}]\}. \tag{21}$$

Here $x[\hat{t}]$, $y[\hat{t}]$, and $z[\hat{t}]$ are time sampled forms of $x(t)$, $y(t)$ and $z(t)$, and $\hat{t}$ denotes an integer time index. (If the sampling interval is T, then $t = \hat{t}T$.) The discrete version of $X(f)$ is the DFT of $x[\hat{t}]$,

$$X[\hat{f}] = \sum_{\hat{t}=0}^{N-1} x[\hat{t}]\exp\left(\frac{-2\pi i\,\hat{f}\hat{t}}{N}\right). \tag{22}$$

Here N denotes the number of samples in the time series, and $\hat{f}$ is an integer frequency index ($f = \hat{f}/NT$). Similar definitions give $Y[\hat{f}]$ and $Z[\hat{f}]$. By sampling eq. (8) in frequency, these quantities can be used to calculate discrete S transforms; that of $x[\hat{t}]$ is (Stockwell *et al.* 1996):

$$\begin{aligned}
X[\hat{\tau}, \hat{f}] = \sum_{\hat{\alpha}=-N/2}^{N/2-1} X[\hat{\alpha} + \hat{f}]\exp\left(\frac{-2\pi^2\hat{\alpha}^2}{\hat{f}^2}\right)\\
\times\exp\left(\frac{2\pi i\hat{\alpha}\hat{\tau}}{N}\right).
\end{aligned} \tag{23}$$

In eq. (23), $\tau = \hat{\tau}T$ and $\alpha = \hat{\alpha}/NT$. Expression (23) is preferable to the time sampled form of eq. (7) for computational reasons (Pinnegar & Mansinha 2003). The discrete S transforms of $y[\hat{t}]$ and $z[\hat{t}]$ have definitions analogous to that of $X[\hat{\tau}, \hat{f}]$ and are denoted $Y[\hat{\tau}, \hat{f}]$ and $Z[\hat{\tau}, \hat{f}]$. These quantities may also be expressed in terms of real and imaginary parts by analogy with eq. (3); for the discrete S transform of $x[\hat{t}]$,

$$X[\hat{\tau}, \hat{f}] = X_R[\hat{\tau}, \hat{f}] + i\ X_I[\hat{\tau}, \hat{f}]. \tag{24}$$

Eqs (19) and (20) then provide a convenient way of defining time–frequency spectra of the elements of the polarization ellipse. By substituting $X_R[\hat{\tau}, \hat{f}], \ldots, Z_I[\hat{\tau}, \hat{f}]$ in place of $X_R(f), \ldots, Z_I(f)$, the discrete S spectra of the elliptical elements, denoted $a[\hat{\tau}, \hat{f}], \ldots, \varphi[\hat{\tau}, \hat{f}]$, are obtained.

3 POLARIZATION ANALYSIS EXAMPLE

For brevity, the $[\hat{\tau}, \hat{f}]$ arguments of discrete S spectra are omitted in this and following sections, except where clarity requires their inclusion. The arguments of all quantities that are not discrete S spectra are retained to reduce ambiguity, e.g. X without arguments represents $X[\hat{\tau}, \hat{f}]$ not $X(f)$.

Fig. 1 shows a segment of a three-component broadband seismogram of an $M = 6.9$ earthquake, recorded at the PEMO seismic

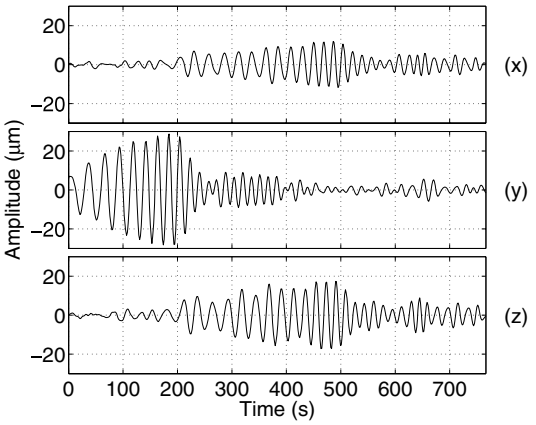

Figure 1. (x) Radial, (y) transverse, and (z) vertical components of a segment of a three-component earthquake seismogram, recorded at the PEMO seismic station in Pembroke, Ontario, Canada on 2003 June 23 (see Section 3 for the details), showing the Love and subsequent Rayleigh phases.

station in Pembroke, Ontario, Canada (45.68°N, 77.25°W). This segment was selected because it contains the Love and Rayleigh phases, which have distinctive polarization properties. The earthquake occurred in the Aleutian Islands (51.58°N, 176.67°E) at a depth of 18 km, on 2003 June 23 at 12:12:35 UT. At the PEMO station the epicentral distance was 7124 km and the azimuth 48.3° north of west. The original data had a sampling interval of 0.01 s and units of velocity (nm/s). This was converted to displacement by integration of the data followed by linear trend removal via least-squares fits to the different components. The resulting seismogram was then decimated to give a new data set with a sampling interval of 1.5 s. (A Butterworth anti-aliasing filter was applied prior to decimation.) The purpose of the decimation was to reduce the size of the *S*-transform matrix for display purposes; at the new sampling frequency, the Love and Rayleigh phases still have about 10–20 samples per cycle. The decimated vertical trace gives the **z** component of the total motion shown in Fig. 1. The **x** and **y** components of Fig. 1 are radial and transverse traces obtained by rotating the decimated easting and northing traces 48.3° counter-clockwise to bring the positive **x**-direction into alignment with the expected direction of wave propagation. The amplitude *S* spectra of these traces, X_A, Y_A and Z_A, are shown in Figs 2–4. In Fig. 3, the first large amplitude event (marked A) is the Love wave arrival; in Figs 2 and 4, the

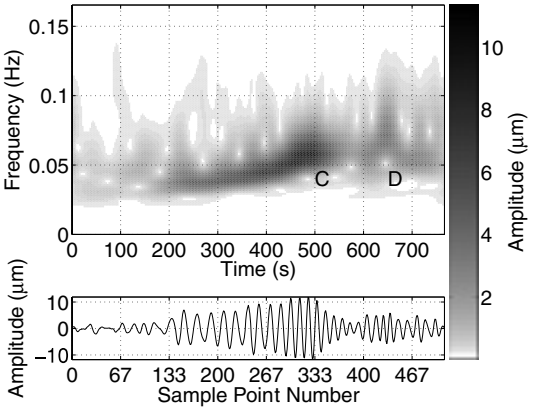

Figure 2. Amplitude *S* spectrum $X[\hat{\tau}, \hat{f}]$ of the **x** component of the seismogram of Fig. 1 (shown in the lower plot). The signatures marked C and D are Rayleigh wave phases.

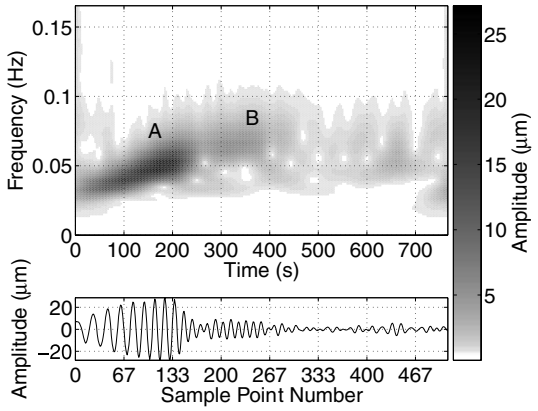

Figure 3. Amplitude *S* spectrum $Y[\hat{\tau}, \hat{f}]$ of the **y** component of the seismogram of Fig. 1 (shown in the lower plot). The signatures marked A and B are Love wave phases.

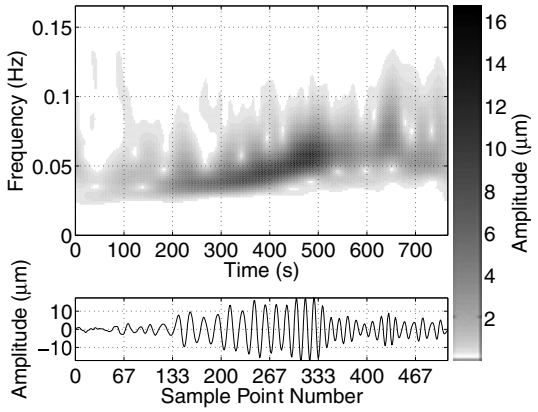

Figure 4. Amplitude *S* spectrum $Z[\hat{\tau}, \hat{f}]$ of the **z** component of the seismogram of Fig. 1 (shown in the lower plot), showing similarities with Fig. 2 and low vertical amplitude of the Love wave phases from Fig. 3.

largest amplitudes (marked C on Fig. 2) are the Rayleigh wave arrival. The lower amplitude events marked D and B on Figs 2 and 3 have Love and Rayleigh properties, respectively; these may represent higher-order phases, or, alternatively, crustal wave packets of relatively high frequency whose shallow penetration depths have delayed their arrival times.

Figs 5 and 6 show the semi-major axis and semi-minor axis *S* spectra, a and b. Their difference, $(a - b)$, is shown in Fig. 7. Since the total polarization ellipse can be thought of as a pure linear motion of amplitude $(a - b)$ that is phase-locked with, and lies in the plane of, a pure circular motion of amplitude b to which it is added, Figs 6 and 7 can be considered as circular-motion and linear-motion *S* spectra. Thus the very low Love wave amplitude in Fig. 6 is a consequence of nearly linear particle motion. The Rayleigh wave signature on Fig. 5 has about 1.5 times the amplitude of the corresponding signature on Fig. 6, leading to a linear-motion amplitude on Fig. 7 that is about half that of Fig. 6. Fig. 8 shows the 'total power' *S* spectrum, defined by $\sqrt{a^2 + b^2}$, or [in the notation of eq. (19)] $\sqrt{A}$.

The *S* spectra of the other four elliptical elements (shown in Figs 9–12) can be difficult to interpret visually because, unlike the *S* spectra in Figs 2–7, they do not give any information about where, on the $[\hat{\tau}, \hat{f}]$ plane, the most significant contributions to the total signal are made. (In this respect they are similar to the Fourier phase

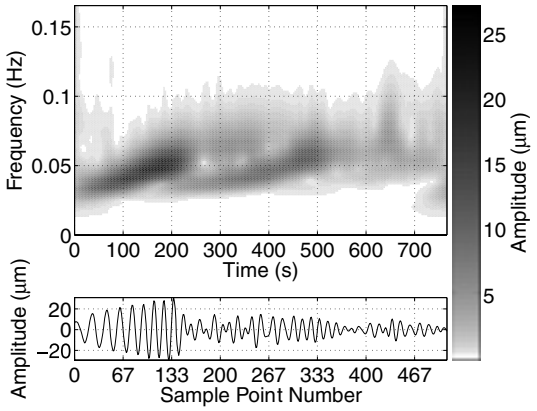

Figure 5. Semi-major axis S spectrum $a[\hat{\tau}, \hat{f}]$ of the seismogram of Fig. 1. This S spectrum gives the time–frequency dependence of the long axis of the polarization ellipse. In this figure and Figs 6–12, the trace shown in the lower plot is the sum of the **x** and **y** components of the seismogram; these have been combined to show both the Love and Rayleigh events in one trace.

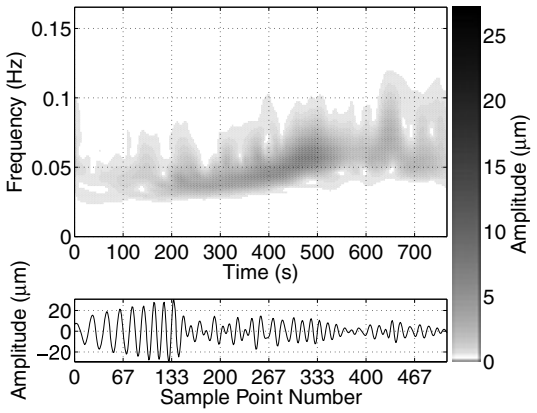

Figure 6. Semi-minor axis S spectrum $b[\hat{\tau}, \hat{f}]$ of the seismogram of Fig. 1. This S spectrum gives the time–frequency dependence of the short axis of the polarization ellipse, and can be thought of as the spectrum of the 'circular' part of the elliptical motion (compare with Fig. 7).

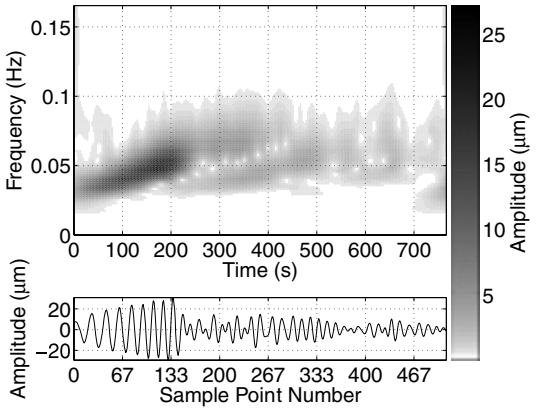

Figure 7. Difference of the semi-major axis and semi-minor axis S spectra $a[\hat{\tau}, \hat{f}] - b[\hat{\tau}, \hat{f}]$ of the seismogram of Fig. 1. This S spectrum can be thought of as the spectrum of the 'linear' component of the elliptical motion (compare with Fig. 6).

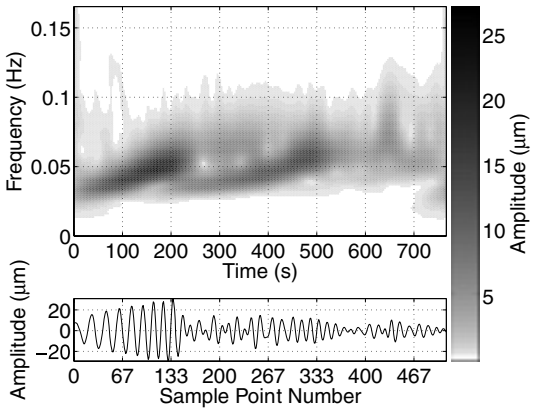

Figure 8. Total-power S spectrum $\sqrt{a[\hat{\tau}, \hat{f}]^2 + b[\hat{\tau}, \hat{f}]^2}$ of the seismogram of Fig. 1. This gives an estimate of energy density that takes all three orthogonal components of the signal into account.

spectra of one-component signals.) To this end, in each of Figs 9–12, the amplitude at each pixel is denoted by one of two different shades of the same colour. The brighter shades are assigned to pixels whose total power (on Fig. 8) is larger than 7 μm; this cut-off value is convenient for outlining the main Love and Rayleigh signatures. The resulting inclination S spectrum I is shown in Fig. 9. For the Rayleigh wave signature, $I \sim \pi/2$, which demonstrates that the plane of the time-local polarization ellipse is nearly vertical (not an unexpected result). The value of I is reasonably stable over the extent of the Rayleigh wave signature on the $[\hat{\tau}, \hat{f}]$ plane; however, on the Love wave signature, I takes on a large range of values. This happens because, for nearly linear simple harmonic particle motion, even small noise contributions can lead to large changes in I (keep in mind that I is the dip of the ellipse plane, not the plunge of the major axis). In the extreme case of purely linear motion,

$$\frac{X_I}{X_R} = \frac{Y_I}{Y_R} = \frac{Z_I}{Z_R}, \tag{25}$$

so I, Ω, and consequently ω are undefined, because terms of the form $Z_R Y_I - Z_I Y_R$ are equal to 0 in eq. (20). Purely linear motion is unlikely to be encountered in real seismograms, since noise contamination will always introduce some ellipticity, but this limitation of the method should be borne in mind when working with synthetic seismograms.

The azimuth of the ascending node S spectrum, Ω, is shown in Fig. 10. As in Fig. 9, the nearly linear particle motion of the Love wave leads to instability because noise can easily reverse the direction of particle motion from counter-clockwise to clockwise and vice versa, causing Ω to suddenly change by $\pm\pi$. Here Ω is roughly $\pi/2$ or $-\pi/2$, which is not surprising since for Love waves the strike of the local polarization ellipse should be perpendicular to the direction of wave propagation. On the Rayleigh wave signature, Ω has a relatively stable value near zero, which means that the particle is displaced in the direction of wave propagation when it crosses the horizontal plane in the positive **z**-direction. This demonstrates the retrograde motion of the Rayleigh wave. (These values of Ω can be roughly estimated from visual inspection of the time series in Fig. 1: on the Love wave trains, only $y[\hat{t}]$ has much amplitude; and, on the Rayleigh wave trains, $x[\hat{t}]$ is positive near the ascending zero crossings of $z[\hat{t}]$, while $y[\hat{t}]$ has small amplitude by comparison.)

Since Love wave motion is almost completely horizontal and linear, its largest displacement from $\{0, 0, 0\}$ should be close to either the ascending node or the descending node. Thus the S spectrum of the argument of maximum, ω, should be either nearly zero, or nearly π, on the Love wave signature. This can be seen in Fig. 11. For the

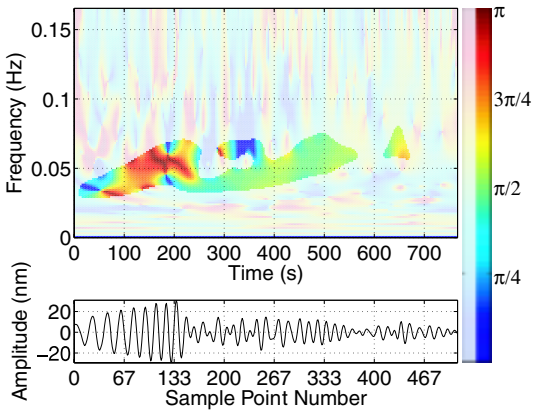

Figure 9. Inclination S spectrum $I[\hat{\tau}, \hat{f}]$ of the seismogram of Fig. 1. This S spectrum gives the time–frequency dependence of the 'dip' of the ellipse plane relative to the horizontal. Brighter colours are used to denote values of $\hat{\tau}$ and $\hat{f}$ at which the total power (shown in Fig. 8) is larger than 7 μm.

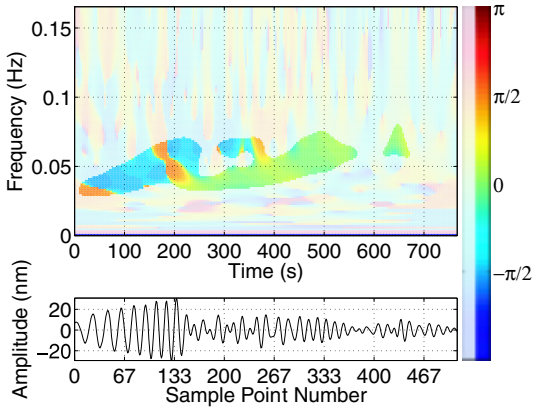

Figure 10. Azimuth of ascending node S spectrum $\Omega[\hat{\tau}, \hat{f}]$ of the seismogram of Fig. 1. This S spectrum gives the time–frequency dependence of the 'strike' of the ellipse plane. Brighter colours are used to denote values of $\hat{\tau}$ and $\hat{f}$ at which the total power (shown in Fig. 8) is larger than 7 μm.

Rayleigh wave train, ω is almost exactly $\pi/2$, which is also not surprising since the long axis of the polarization ellipse of a Rayleigh wave is normally nearly vertical. The phase S spectrum, φ, shown in Fig. 12, is not well suited for visual interpretation. However, φ is still important because, without the phase information, $\mathbf{r}[\hat{t}]$ cannot be reconstructed from the information in a, b, I, Ω, and ω.

The seismic trace used above was chosen to illustrate the technique because of its low noise content. The method is however actually fairly robust in the presence of moderate amounts of noise. When Gaussian white noise is added to the data to give a signal-to-noise ratio (SNR) of approximately 1, the Love and Rayleigh signatures are still clearly visible on the a and b S spectra, and retain recognizable (though distorted) polarization properties on the I, Ω and ω S spectra.

4 POLARIZATION FILTERING

4.1 'Linear' and 'circular' traces

Through use of the methodology outlined above, $\mathbf{r}[\hat{t}]$ can be divided into two three-component time series that, in some sense, describe the time evolution of the separate linear and circular parts of the

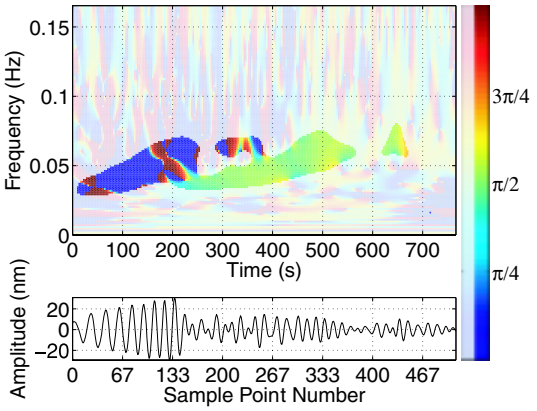

Figure 11. Argument of maximum S spectrum $\omega[\hat{\tau}, \hat{f}]$ of the seismogram of Fig. 1. This S spectrum gives the time–frequency dependence of the 'pitch' of the major axis of the ellipse. Brighter colours are used to denote values of $\hat{\tau}$ and $\hat{f}$ at which the total power (shown in Fig. 8) is larger than 7 μm.

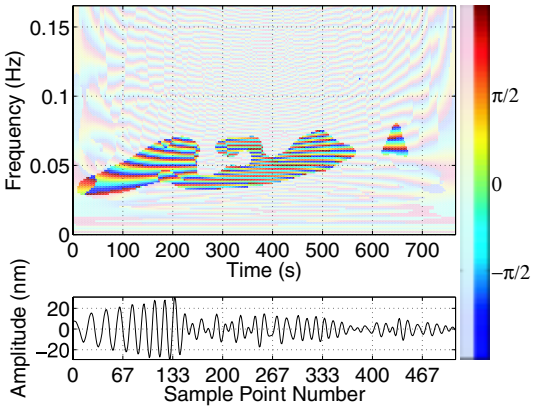

Figure 12. Phase S spectrum $\varphi[\hat{\tau}, \hat{f}]$ of the seismogram of Fig. 1. Brighter colours are used to denote values of $\hat{\tau}$ and $\hat{f}$ at which the total power (shown in Fig. 8) is larger than 7 μm.

trace. (Readers who wish to skip the mathematical details of this can proceed to the example shown in Section 4.2.) This is done by first returning to continuous time and rewriting eq. (13) so that the linear and circular parts of the test ellipse are separated from each other before being rotated, to give

$$\mathbf{r}'(t) = [a(f) - b(f)]\{\cos[2\pi ft - \varphi(f)], 0, 0\} + b(f)\,\{\cos[2\pi ft - \varphi(f)], \sin[2\pi ft - \varphi(f)], 0\}. \quad (26)$$

When the approach of eqs (14)–(18) is applied to eq. (26) and the results considered in the $[\hat{\tau}, \hat{f}]$ domain, each of $X_R, \ldots, Z_I$ turns out to be the sum of two parts that describe the linear and circular parts of $\mathbf{r}(t)$; these are denoted by L and C superscripts. As an example,

$$\begin{aligned} X_R &= X_R^L + X_R^C, \text{ where} \\ X_R^L &= [a - b]\ \cos\varphi(\cos\omega\cos\Omega - \sin\omega\sin\Omega\cos I), \\ X_R^C &= b[\cos\varphi(\cos\omega\cos\Omega - \sin\omega\sin\Omega\cos I) \\ &\quad + \sin\varphi(\sin\omega\cos\Omega + \cos\omega\sin\Omega\cos I)]. \end{aligned} \quad (27)$$

The linear and circular parts of the other quantities from eq. (18) have similar definitions. The simplest way of evaluating $X_R^L, \ldots, Z_I^C$ numerically is to calculate $a, \ldots, \varphi$ using eqs (19) and (20), then substitute the results into the expressions of $X_R^L, \ldots, Z_I^C$.

The invertibility condition of the discrete S transform, equivalent to eq. (9) sampled in frequency, is

$$X[\hat{f}] = \sum_{\hat{\tau}=0}^{N-1} X[\hat{\tau}, \hat{f}], \text{ or}$$
$$= \sum_{\hat{\tau}=0}^{N-1} X_R[\hat{\tau}, \hat{f}] + i\, X_I[\hat{\tau}, \hat{f}]. \quad (28)$$

From eqs (27) and (28), linear and circular parts of $X[\hat{f}]$, denoted $X^L[\hat{f}]$ and $X^C[\hat{f}]$, can be obtained via

$$X[\hat{f}] = X^L[\hat{f}] + X^C[\hat{f}], \text{ where}$$
$$X^L[\hat{f}] = \sum_{\hat{\tau}=0}^{N-1} X_R^L[\hat{\tau}, \hat{f}] + i X_I^L[\hat{\tau}, \hat{f}]$$
$$X^C[\hat{f}] = \sum_{\hat{\tau}=0}^{N-1} X_R^C[\hat{\tau}, \hat{f}] + i X_I^C[\hat{\tau}, \hat{f}]. \quad (29)$$

The inverse Fourier transforms of $X^L[\hat{f}]$ and $X^C[\hat{f}]$ give $x^L[\hat{t}]$ and $x^C[\hat{t}]$, the linear and circular parts of $x[\hat{t}]$. Through similar reasoning, one can obtain the linear and circular parts of $y[\hat{t}]$ and $z[\hat{t}]$ and, consequently, of $\mathbf{r}[\hat{t}]$.

4.2 Example

A useful shorthard notation is to denote the whole inverse operation of the S spectra of the elliptical elements, as described in eqs (26)–(29), by Q, so that

$$\mathbf{r}[\hat{t}] = \mathbf{r}^L[\hat{t}] + \mathbf{r}^C[\hat{t}] = Q(a, b, I, \Omega, \omega, \varphi),$$
$$\mathbf{r}^L[\hat{t}] = Q(a - b, 0, I, \Omega, \omega, \varphi),$$
$$\mathbf{r}^C[\hat{t}] = Q(b, b, I, \Omega, \omega, \varphi). \quad (30)$$

Fig. 13 shows hodograms of the linear part $\mathbf{r}^L[\hat{t}]$ (black lines) and the circular part $\mathbf{r}^C[\hat{t}]$ (grey lines) of the seismogram from Fig. 1. Each row of hodograms shows a different time segment as viewed from the positive **x**-, **y**-, and **z**-directions. The first row shows the Love wave motion in the first part of the time series. In the second row, Love wave and Rayleigh wave motion are mixed together; the direction of radial motion changes gradually from horizontal to vertical, and circular motion increases in amplitude. The third row shows Rayleigh wave motion near its maximum amplitude, and the fourth row shows the Rayleigh wave coda. The various segments of these time series are of course not purely linear or purely circular (if they were, $\mathbf{r}^L[\hat{t}]$ could not change direction and $\mathbf{r}^C[\hat{t}]$ could not change amplitude) but in most cases are approximately so. One exception is the view from the position **x**-direction shown in the second row, in which the superposition of the linear parts of the Love and Rayleigh wave motions (which are roughly perpendicular to each other and have different frequencies at these times) leads to $\mathbf{r}^L[\hat{t}]$ tracing out 'figure-of-eight'-like motion. Over short time periods this motion can appear to be circular, but usually reverses direction before making a complete cycle around the origin. This type of behaviour for $\mathbf{r}^L[\hat{t}]$ is quite common in multicomponent traces. Similarly, under the right circumstances the motion of $\mathbf{r}^C[\hat{t}]$ can take on an epicycloidal appearance that may briefly appear to be linear, but which usually reverses direction before passing through the origin.

4.3 Time–frequency filtering of Rayleigh waves

The elliptical elements $a, \ldots, \varphi$ are also useful in time–frequency filter design [some previous examples of time–frequency filtering with the S transform are described in Pinnegar & Eaton (2003) and Pinnegar (2005)]. In the following example, Rayleigh wave motion is removed from the earthquake trace by applying a time–frequency filter whose rejection regions are times and frequencies for which $I \sim \pi/2$, $\omega \sim 0$, and $b \gtrsim a/2$. Fig. 14 shows the functions F_1, F_2 and F_3 that are used to construct the filter, plotted as continuous functions of their arguments. Their definitions are

$$F_1(I) = 0, \left| I - \frac{\pi}{2} \right| < \frac{\pi}{10}$$
$$= \frac{1 - \cos(10|I - \frac{\pi}{2}| - \pi)}{2}, \frac{\pi}{10} \le \left| I - \frac{\pi}{2} \right| \le \frac{\pi}{5}$$
$$= 1, \left| I - \frac{\pi}{2} \right| > \frac{\pi}{5},$$
$$F_2(b/a) = 1, b < 0.5a,$$
$$= \frac{1 + \cos[10\pi\,(b/a - 0.5)]}{2}, 0.5a \le b \le 0.6a,$$
$$= 0, b > 0.6a$$
$$F_3(\Omega) = 0, |\Omega| < \frac{\pi}{6},$$
$$= \frac{1 - \cos(6|\Omega| - \pi)}{2}, \frac{\pi}{6} \le |\Omega| \le \frac{\pi}{3}$$
$$= 1, |\Omega| < \frac{\pi}{3}. \quad (31)$$

Here the cosine tapers of F_1, F_2 and F_3 give the total time–frequency filter F its frequency-dependent Fourier-domain taper. F is obtained by substituting the a, b, I, and Ω S spectra into eq. (31) at all $[\hat{\tau}, \hat{f}]$ positions, with

$$F[\hat{\tau}, \hat{f}] = 1 - \{1 - F_1(I[\hat{\tau}, \hat{f}])\}\left\{1 - F_2\left(\frac{b[\hat{\tau}, \hat{f}]}{a[\hat{\tau}, \hat{f}]}\right)\right\}$$
$$\times \{1 - F_3(\Omega[\hat{\tau}, \hat{f}])\}. \quad (32)$$

Expression (32) ensures that the only parts of the $[\hat{\tau}, \hat{f}]$ plane that are rejected by F are those that are rejected by all three of F_1, F_2, and F_3. Fig. 15 shows $F_1(I[\hat{\tau}, \hat{f}])$, $F_2(b[\hat{\tau}, \hat{f}]/a[\hat{\tau}, \hat{f}])$, $F_3(\Omega[\hat{\tau}, \hat{f}])$ and the total filter F for the earthquake trace of Fig. 1. [The ratio b/a, around which F_2 is designed, is conceptually similar to rectilinearity functions used by Montalbetti & Kanasewich (1970), Vidale (1986), and Jurkevics (1988)]. One way of filtering the trace would be to simply multiply X, Y and Z by F and invert the result through use of eq. (28). This actually produces good results, but a more interesting approach is to assume that each ellipse can be decomposed (in analogy with section 4.1) into two parts: a Rayleigh-type wave motion whose minor axis is equal to that of the original ellipse and for which $a/b = 1.5$; and residual linear motion of amplitude $a - 1.5b$ that is assumed to be unassociated with the Rayleigh wave. The amount of Rayleigh-type wave motion retained at each $[\hat{\tau}, \hat{f}]$ is determined by F. The resulting filtered trace is denoted $\mathbf{r}^F[\hat{t}]$; in the shorthand notation of eq. (30),

$$\mathbf{r}^F[\hat{t}] = Q(a - 1.5b(1 - F), bF, I, \Omega, \omega, \varphi). \quad (33)$$

Fig. 16 shows the filtered earthquake seismogram along with the original data from Fig. 1 for comparison. The Rayleigh wave has been almost completely removed from the trace. In most of the parts of the trace that have experienced large amplitude reductions, the remaining signal has a frequency that is closer to that of the Love wave. The exception is the part of the trace from 600 to 700 s where some Rayleigh wave amplitude, related to the event marked D on Fig. 2, has been retained. For this event,

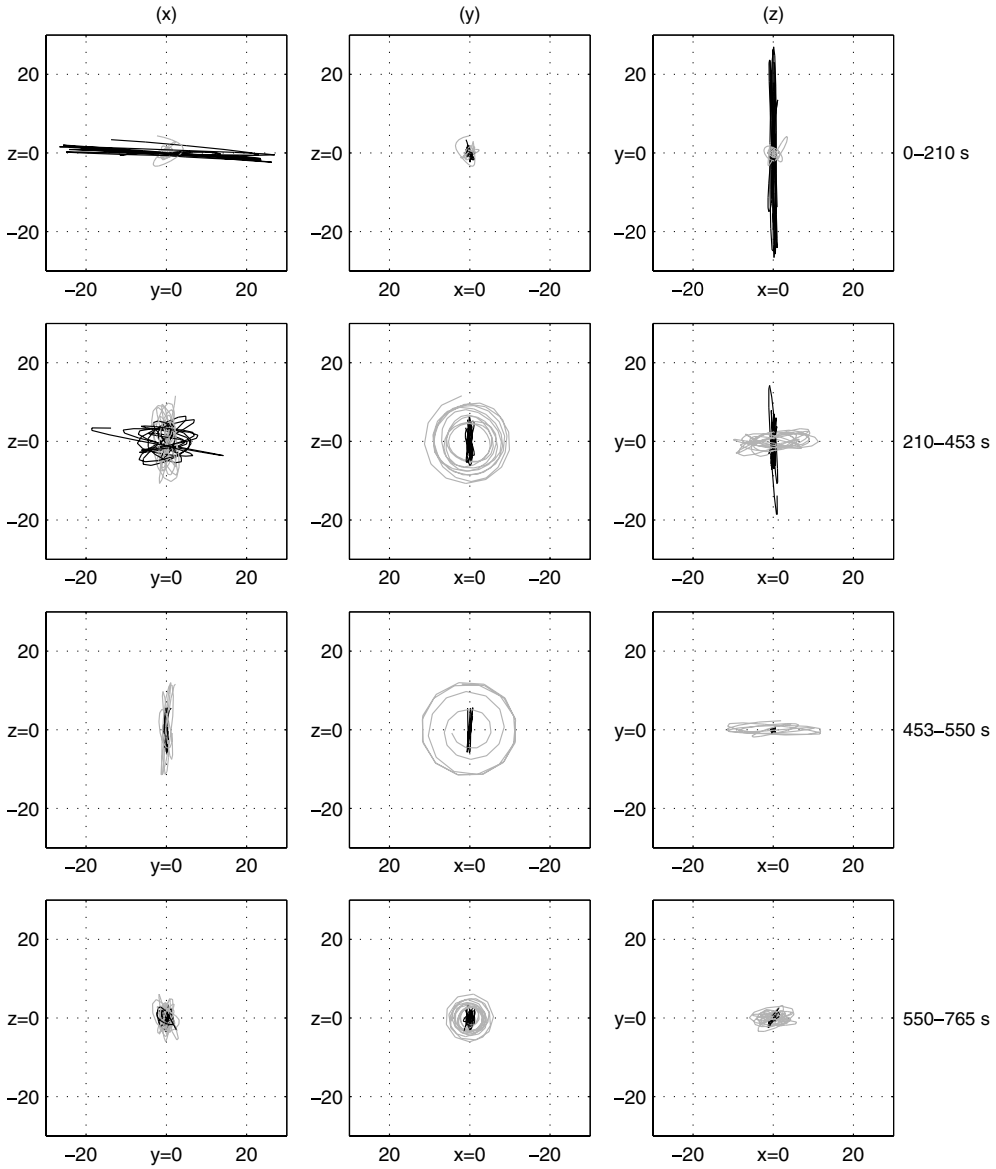

Figure 13. Linear (black lines) and circular (grey lines) parts of the seismogram shown in Fig. 1 (denoted $\mathbf{r}^L[\hat{t}]$ and $\mathbf{r}^C[\hat{t}]$ in the text), obtained through polarization filtering. The three columns denote views from the positive **x**-, **y**-, and **z**-directions; the four rows indicate different segments of the seismogram, showing, in succession, the Love phase, the Love phase coda with concurrent main Rayleigh phase arrival, the main Rayleigh phase after attenuation of the Love phase, and the Rayleigh phase coda. All displacements shown have units of μm.

I strays farther from $\pi/2$ than in the main part of the Rayleigh wave (see Fig. 9), which allows some of its energy to be passed by the filter.

Although the elliptical elements $a, \ldots, \varphi$ are useful for designing time–frequency filters, they are not the only quantities on which filters can be based. For example, a filter could be designed to reject specific values of the altitude θ and azimuth ζ (i.e. the plunge and trend) of the major axis of the polarization ellipse. These can be obtained from

$$\begin{aligned} \sin(\theta) &= \sin(I)\sin(\omega), \\ \tan(\zeta) &= \frac{\tan(\Omega) + \tan(\omega)\tan(I)}{1 - \tan(\Omega)\cos(I)\tan(\Omega)}. \end{aligned} \tag{34}$$

4.4 Trace-by-trace filtering of shot gathers

Fig. 17(a) shows the vertical component of a three-component shot gather to which automatic gain correction (AGC) has been applied. For this data set the sampling interval is 2 ms and the receiver interval 5 m. AGC was applied by dividing each uncorrected $\{x[\hat{t}], y[\hat{t}], z[\hat{t}]\}$ trace in the gather by its estimated instantaneous amplitude, using

$$\{x^c[\hat{t}], y^c[\hat{t}], z^c[\hat{t}]\} = \frac{\{x[\hat{t}], y[\hat{t}], z[\hat{t}]\}}{\sqrt{|\tilde{x}[\hat{t}]|^2 + |\tilde{y}[\hat{t}]|^2 + |\tilde{z}[\hat{t}]|^2} \star g(t)}. \tag{35}$$

Here $x^c[\hat{t}]$, $y^c[\hat{t}]$, $z^c[\hat{t}]$ are the components of the trace after AGC, and $\tilde{x}[\hat{t}]$, $\tilde{y}[\hat{t}]$, $\tilde{z}[\hat{t}]$ are complex analytic signals obtained from $x[\hat{t}]$, $y[\hat{t}]$, $z[\hat{t}]$ and their Hilbert transforms. (Thus the data shown

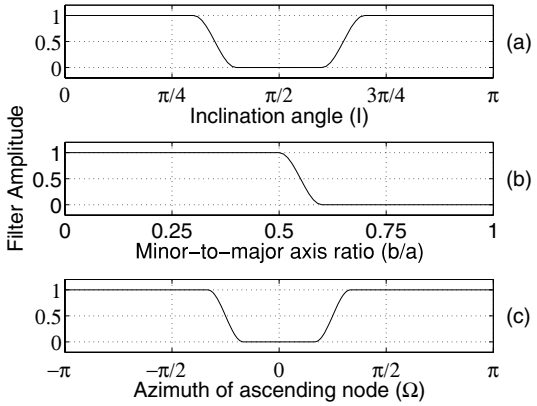

Figure 14. Response of (a) F_1, (b) F_2, and (c) F_3 elliptical element-based filters; their definitions appear in expression (31).

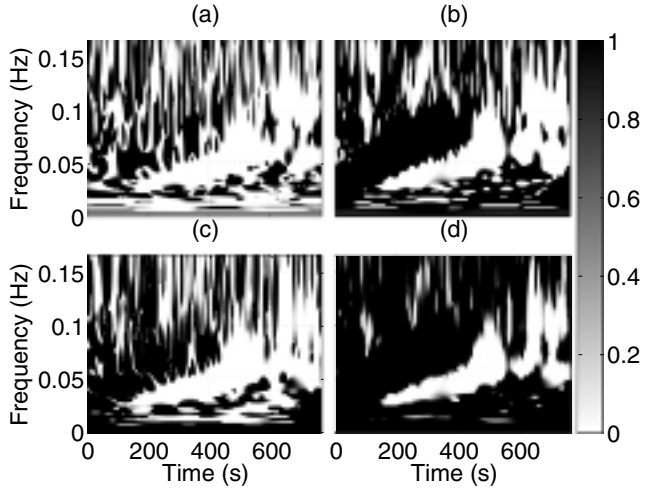

Figure 15. Time–frequency filters obtained by substituting the data values from the time–frequency spectra shown in Figs 5, 6, 9, and 10 into the filters shown in Fig. 14, to give (a) $F_1(I[\hat{\tau}, \hat{f}])$, (b) $F_2(b[\hat{\tau}, \hat{f}]/a[\hat{\tau}, \hat{f}])$, and (c) $F_3(\Omega[\hat{\tau}, \hat{f}])$. (d) Total time–frequency filter $F[\hat{\tau}, \hat{f}]$ thus obtained from eq. (32). This filter targets the parts of Fig. 1 that have Rayleigh-type wave motion.

in Fig. 17 is dimensionless; the original data had units of velocity.) The $g[\hat{t}]$ function is a Gaussian with a standard deviation of 100 ms, that is convolved with the modulus of $\{\tilde{x}[\hat{t}], \tilde{y}[\hat{t}], \tilde{z}[\hat{t}]\}$ to give a smoothed signal envelope (here $\star$ denotes convolution). Fig. 17(b) shows the same shot gather after trace-by-trace filtering using the technique and filters described in the previous subsection, and subsequent AGC. Almost all of the Rayleigh wave motion has been removed from the gather.

As a second example, Fig. 18(a) shows the vertical component of a three-component shot gather, acquired by the CREWES Project at the University of Calgary over the Encana Corp. Blackfoot oilfield area in Alberta, Canada. For this data set the sampling interval is again 2 ms but the receiver interval is 60 m. The only change in the filter design is a translation of F_3 that centres its rejection region around $\Omega = \pi/6$, to accommodate the ground roll characteristics of this particular shot gather. As in the previous example, AGC was applied to each trace after filtering. From visual inspection of Fig. 18(b) we can see that much of the Rayleigh ground roll has been removed from the shot gather, although some has been retained (particularly at larger offsets). Hodograms of specific trace

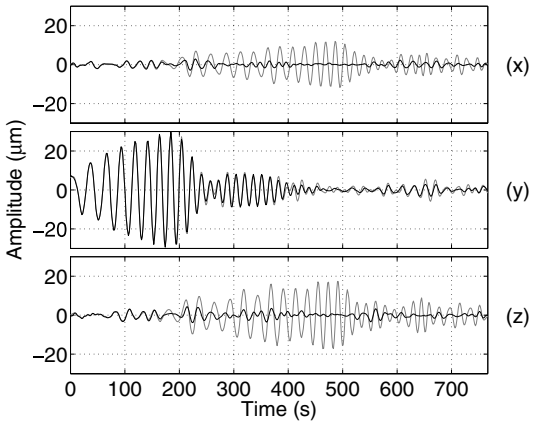

Figure 16. (*x*) Radial, (*y*) transverse, and (*z*) vertical components of the data in Fig. 1 before (grey lines) and after (black lines) application of the filter of Fig. 15(d), showing selective removal of the Rayleigh phases.

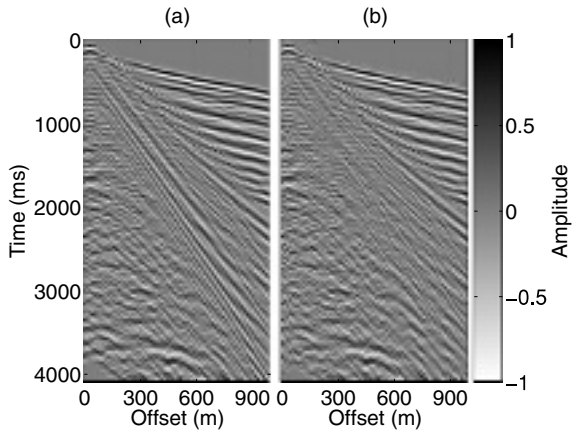

Figure 17. (a) Automatic gain corrected shot gather (see Section 4.4 for the details). (b) The same shot gather after the filters shown in Fig. 14 have been applied to each trace before gain correction. Most of the Rayleigh-phase ground roll has been removed from the gather.

segments from Fig. 18(a) appear in Figs 19(a)–(c), which show the trace at 300 m offset from $t = 0.6$ to 1 s; the trace at 360 m offset from $t = 0.8$ to 1.2 s; and the trace at 420 m offset from $t = 1$ to 1.3 s. The start and end times of these segments, which show the complexity of the particle motion for this data set, have been chosen so that each contains the largest amplitude of the Rayleigh wave. Figs 19(d)–(f) show the same three trace segments after filtering. The filter performs best in the trace segment of Figs 19(b) and (e) but also removes some ground roll from the other two segments.

5 CONCLUSIONS

I have presented a method that uses the *S* transform of Stockwell *et al.* (1996) to produce time–frequency spectra of the polarization characteristics of three-component seismic signals: the semi-major and semi-minor axes of the polarization ellipse, the strike and dip of the ellipse plane, the pitch of the major axis, and the phase of the particle motion. These spectra can be used to divide the whole signal into 'linear' and 'circular' parts, and to construct signal-adaptive time–frequency filters that target specific types of particle motion such as the Rayleigh wave. The method has potential utility in

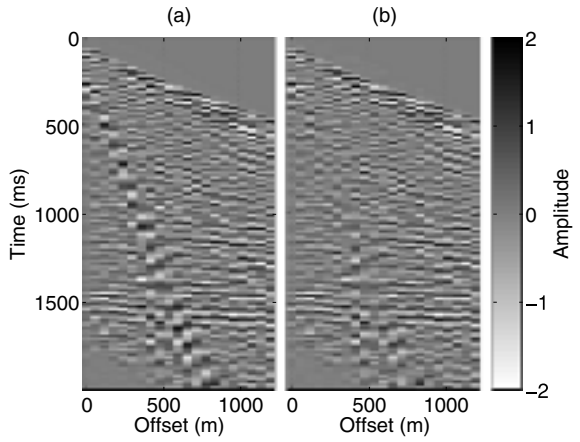

Figure 18. (a) Automatic gain corrected shot gather from the Blackfoot region of Alberta, Canada (see section 4.4 for the details). (b) The same shot gather after filters similar to those shown in Fig. 14 have been applied to each trace before gain correction (the only difference is that the centre of the rejection region of F_3 from Fig. 14(c) has been translated to $\Omega = \pi/6$). Much of the Rayleigh-phase ground roll has been removed from the gather.

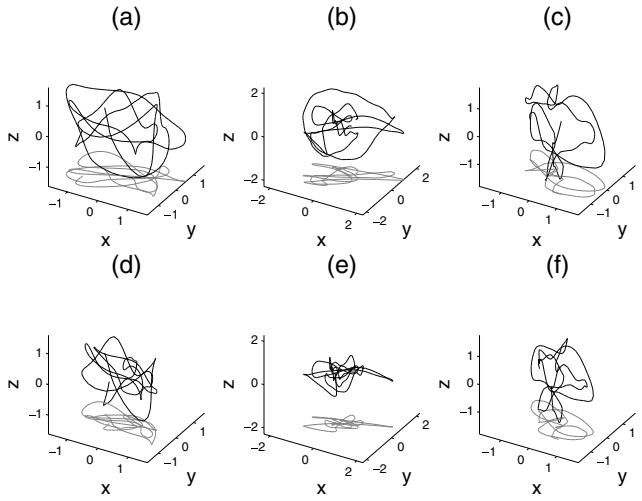

Figure 19. Hodograms of trace segments from: Fig. 18(a) at (a) 300 m offset, from 0.6 to 1 s; (b) 360 m offset, from 0.8 to 1.2 s; (c) 420 m offset, from 1 to 1.3 s; and (d–f) from Fig. 18(b) at the same three times and offsets. In each hodogram the projection of the particle motion onto the $\mathbf{x} - \mathbf{y}$ plane is shown in grey as a 'shadow' beneath the main trace, to give a better idea of the total motion in 3-space. The filter performs best at 360 m offset, but removes some ground roll from all three traces.

earthquake and exploration seismology, and any other application that involves analysis of three-component signals.

ACKNOWLEDGMENTS

It is a pleasure to thank David Eaton, Bob Mereu, Lalu Mansinha, and Savka Dineva at University of Western Ontario for providing a number of helpful suggestions during the course of this research, and for helping to interpret the seismogram (which was provided by the Polaris seismic network). David Eaton also reviewed a draft version of the manuscript. I also thank Rob Stewart, Gary Margrave and the CREWES consortium at University of Calgary for helpful discussions and for allowing use of the Blackfoot data. The shot gather of Fig. 17(a) was provided by an oil and gas company that have requested anonymity. I gratefully acknowledge their contribution.

REFERENCES

Aki, K. & Richards, P.G., 1980. *Quantitative seismology: Theory and methods*, W.H. Freeman, San Francisco.

Anant, K.S. & Dowla, F.U., 1997. Wavelet transform methods for phase identification in three-component seismograms, *Bull. seism. Soc. Am.,* **87,** 1598–1612.

Claassen, J.P., 2001. Robust bearing estimation for three-component stations, *Pure. appl. Geophys.,* **158,** 349–374.

Cohen, L., 1995. *Time-frequency analysis*, Prentice-Hall, Englewood Cliffs, New Jersey.

Flinn, E.A., 1965. Signal analysis using rectilinearity and direction of particle motion, *Proc. IEEE,* **53,** 1874–1876.

Gabor, D., 1946. Theory of communications, *J. Inst. Elec. Eng.,* **93,** 429–457.

Grossmann, A. & Morlet, J., 1984. Decomposition of Hardy functions into square integrable wavelets of constant shape, *SIAM J. Math. Anal.,* **15,** 723–736.

Jurkevics, A., 1988. Polarization analysis of three-component array data, *Bull. seism. Soc. Am.,* **78,** 1725–1743.

Kanasewich, E.R., 1981. *Time sequence analysis in geophysics*, University of Alberta Press, Edmonton.

Lay, T. & Wallace, T.C., 1995. *Modern Global Seismology*, Academic Press, San Diego.

Lilly, J.M. & Park, J., 1995. Multiwavelet spectral and polarization analysis of seismic records, *Geophys. J. Int.,* **122,** 1001–1021.

Mallat, S., 1998. *A Wavelet Tour of Signal Processing*, Academic Press, London, UK.

Montalbetti, J.F. & Kanasewich, E.R., 1970. Enhancement of teleseismic body phases with a polarization filter, *Geophys. J. R. astr. Soc.,* **21,** 119–129.

Morozov, I.B. & Smithson, S.B., 1996. Instantaneous polarization attributes and directional filtering, *Geophysics,* **61,** 872–881.

Murray, C.D. & Dermott, S.F., 1999. *Solar system dynamics*, Cambridge University Press, New York.

Pinnegar, C.R., 2005. Time-frequency and time-time filtering with the S transform and TT transform, *Dig. Signal Process.,* **15,** 604–620.

Pinnegar, C.R. & Eaton, D.W., 2003. Application of the S-transform to prestack noise attenuation filtering, *J. Geophys. Res. – Solid Earth,* **108,** no. 2422.

Pinnegar, C.R. & Mansinha, L., 2003. The bi-Gaussian S-transform, *SIAM J. Sci. Comput.,* **24,** 1678–1692.

Samson, J.C. & Olson, J.V., 1980. Some comments on the descriptions of the polarization states of waves, *Geophys. J. R. astr. Soc.,* **61,** 115–129.

Simons, R.S., 1968. A surface wave particle motion discrimination process, *Bull. seism. Soc. Am.,* **58,** 629–637.

Stockwell, R.G., Mansinha, L. & Lowe, R.P., 1996. Localization of the complex spectrum: The S transform, *IEEE Trans. Signal Process.,* **44,** 998–1001.

Vidale, J.E., 1986. Complex polarization analysis of particle motion, *Bull. seism. Soc. Am.,* **76,** 1393–1405.

Zanandrea, A., Neto, C.R., Rosa, R.R. & Ramos, F.F., 2000. *Physica A,* **283,** 175–180.